Miniature Pneumatic Actuators for Soft Robots by High-Resolution Multimaterial 3D Printing

*Yuan-Fang Zhang, Colin Ju-Xiang Ng, Zhe Chen, Wang Zhang, Sahil Panjwani, Kavin Kowsari, Hui Ying Yang, and Qi Ge**

Miniature soft robots offer excellent safety and deformability, which are highly desirable in applications such as navigation in confined areas or the manipulation of microscale objects. However, it is difficult to manufacture such robots using traditional processes due to the complexity of their design. While rapidly advancing 3D printing technologies offer manufacturing flexibility, it is still challenging to fabricate soft pneumatic robots on millimeter scales due to the difficulty in making microscale voids and channels, which are essential for pneumatic actuation. A generic process flow for systematic and efficient tailoring of the material formulation and key processing parameters for digital light processing-based 3D printing of miniature pneumatic actuators for soft robots is presented. The process flow includes selection of photoabsorber and material performance characterization to determine the appropriate material formulation and characterizations for curing depth and XY fidelity to identify the combination of exposure time and sliced layer thickness. By applying the tailored results to a self-built multimaterial 3D printing system, an assortment of miniature soft pneumatic robots with various structures and morphing modes are printed. Furthermore, potential applications of printed miniature actuators are exemplified by a soft debris remover that navigates in a confined space and collects small objects in a hard-to-reach position.

1. Introduction

Soft robots made of compliant and flexible materials have gained great attention owing to their superior capability of adapting to complex environments and building safe interaction with humans.[1,2] Along with their rapid growth, soft robots have found various applications across multiple length scales from meters to submicrometers.[3–17] Particularly, miniaturized soft robots at millimeter scale with micrometer features are well suited for navigation in confined areas and manipulation of small objects, and therefore promise attractive potentials in applications like jet-engine maintenance, minimally invasive surgery, medical navigation, and others.[18–20] Among all the actuation mechanisms, soft pneumatic robots are of particular interest as they exhibit rapid actuation with large stroke and nearly no friction issues.[21] However, scaling down the designs of soft pneumatic robots to millimeters imposes high requirements on the precision of fabrication on account of the features that are more than one order of magnitude finer.

So far, most miniature soft pneumatic robots are fabricated via traditional manufacturing approaches such as molding and soft lithography which demand great delicacy and constrain structure design to relatively simple geometries.[22–30] As the complexity of design increases, those manufacturing processes become extremely complex and arduous.[31–34] Rapidly advancing 3D printing technologies enable creation of highly complex 3D structures in one single step and have been applied to the fabrication of soft pneumatic robots at centimeter and even larger scales.[5,35–40] Nonetheless, due to the difficulty in making microscale voids and channels which are essential for the pneumatic actuation, successful examples of 3D printing miniature soft pneumatic robots at millimeter scale are rare.[41,42] Among all the existing 3D printing technologies, digital light processing (DLP)-based 3D printing employs localized photopolymerization to create geometrically complex 3D structures from micro- to mesoscales with microscale architecture.[43–45] It is therefore an ideal approach to manufacturing 3D objects with microscale voids and channels. It has already been successfully applied to the fabrication of microfluidic devices with ≈20 μm channels.[46–48] To achieve high printing resolution

Dr. Y.-F. Zhang, C. J.-X. Ng, W. Zhang, S. Panjwani, Dr. K. Kowsari, Prof. H. Y. Yang, Prof. Q. Ge
Digital Manufacturing and Design Centre
Singapore University of Technology and Design
Singapore 487372, Singapore
E-mail: geq@sustech.edu.cn
Z. Chen
Key Laboratory of Soft Machines and Smart Devices
of Zhejiang Province
Department of Engineering Mechanics
Zhejiang University
Hangzhou 310027, China
Prof. Q. Ge
Department of Mechanical and Energy Engineering
Southern University of Science and Technology
Shenzhen 518055, China
Prof. Q. Ge
Centers for Mechanical Engineering Research and Education
at MIT and SUSTech
Southern University of Science and Technology
Shenzhen 518055, China

The ORCID identification number(s) for the author(s) of this article can be found under https://doi.org/10.1002/admt.201900427.

and fidelity in DLP-based 3D printing, it is common practice to add photoabsorber into polymer solutions, which greatly decays light intensity in both lateral and vertical directions. However, 3D printing soft pneumatic robots does not allow users to overly increase the photoabsorber concentration which leads to rapid degradation in the material's mechanical performance, especially the stretchability which is crucial for soft robots undergoing large deformations during pneumatic actuation. When printing with a polymer solution with little or even no photoabsorber, it becomes challenging to find an appropriate combination of printing parameters (i.e., light intensity, exposure time, and layer thickness) which are crucial for controlling the printing resolutions in both lateral and vertical directions. In addition, in many applications of soft robotics, multimaterial designs have been used to enhance the performance and functionality of robotic systems.[5,33,45] However, multimaterial soft pneumatic robots at millimeter scale with micrometer features have not been realized due to the lack of a high-efficiency, high-resolution multimaterial 3D printing system.[49–51]

Here, we present a generic process flow (**Figure 1**) which guides users to tailor not only the formulation of the ultraviolet (UV)-curable elastomer polymer solution that forms soft pneumatic robots exhibiting large deformations but also printing parameters leading to high printing resolution and geometric fidelity at micrometer scale. As shown in Figure 1a, the process flow starts with the selection of an appropriate photoabsorber which is the most efficient and absorbs the most energy at the wavelength of the UV light irradiated from the DLP-based 3D printer used to print soft pneumatic robots.[46,48,52,53] In Figure 1b, we perform mechanical characterizations to investigate the effect of photoabsorber concentration on the mechanical performance of a chosen UV-curable elastomer. The increase in photoabsorber concentration generally results in the decrease in stretchability of the chosen elastomer. Therefore, a moderate concentration of photoabsorber needs to be determined to trade off the efficiency in controlling printing resolution for better stretchability. Once the formulation of the polymer solution is decided, we further determine the critical printing parameters that control the printing resolutions in lateral and vertical directions. As shown in Figure 1c, we first perform the curing depth characterization to find the relationship between exposure time and curing depth. We then conduct the XY fidelity characterization (Figure 1d) to identify the exposure time which ensures the highest printing fidelity in the x-y plane (lateral direction). Finally, based on the conclusions from the curing depth and XY fidelity characterizations, we decide the appropriate sliced layer thickness for the chosen exposure time to prevent either overcuring or undercuring between layers in the vertical direction.
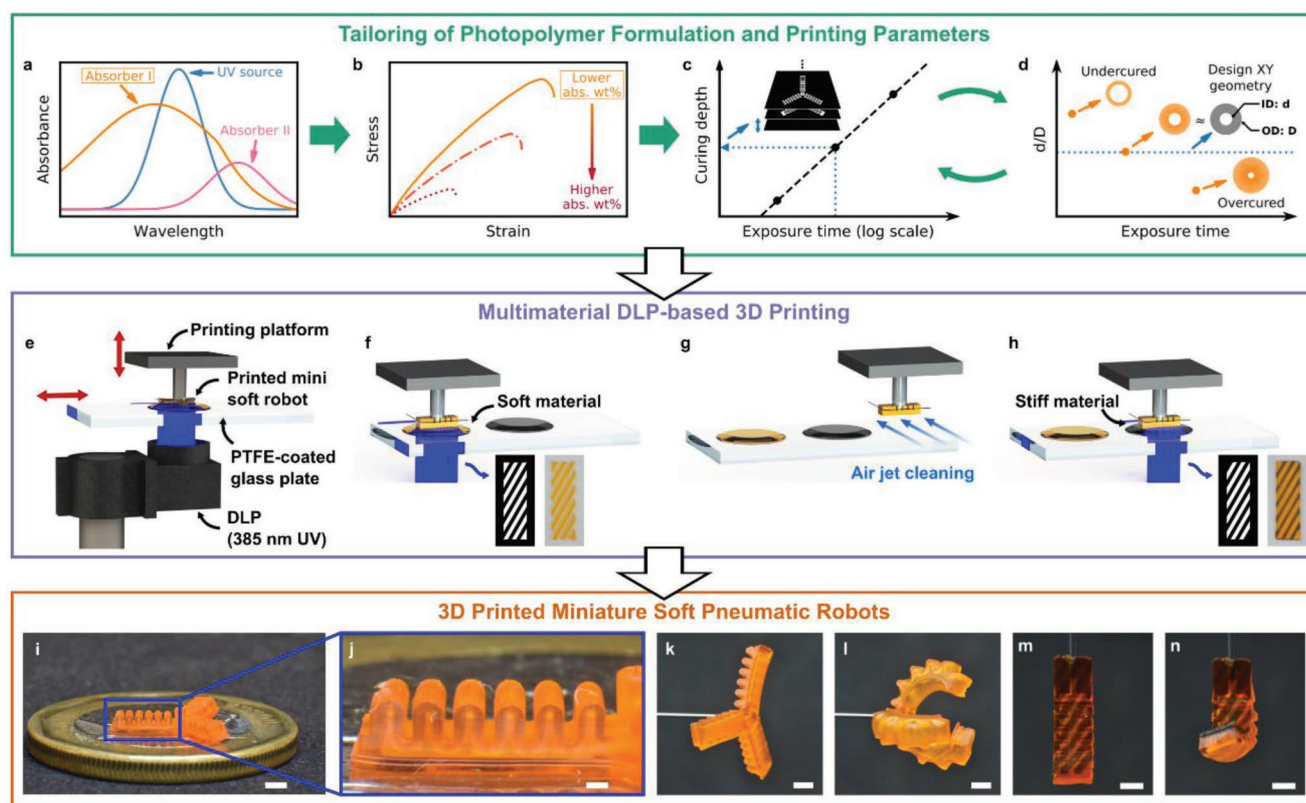

Figure 1. High-resolution 3D printing of miniature soft pneumatic robots. a,b) Material selection based on the efficiency of photoabsorbers and the stretchability of UV-cured elastomer with different absorber concentrations. c,d) Characterizations of curing depth and XY fidelity to identify the appropriate combination of exposure time and sliced layer thickness. e–h) Schematic illustrations of the self-built DLP-based multimaterial 3D printing system that allows rapid material exchange between puddles and cleaning of printed parts with air jet. i,j) Demonstration of a 3D-printed miniature soft pneumatic gripper with distinct channels inside the bellows. k,l) Bending actuation of a 3D-printed miniature gripper. m,n) Helical actuation of a 3D-printed miniature multimaterial actuator. Scale bars: (i) 2 mm; (j) 500 µm; (k)–(n) 2 mm.
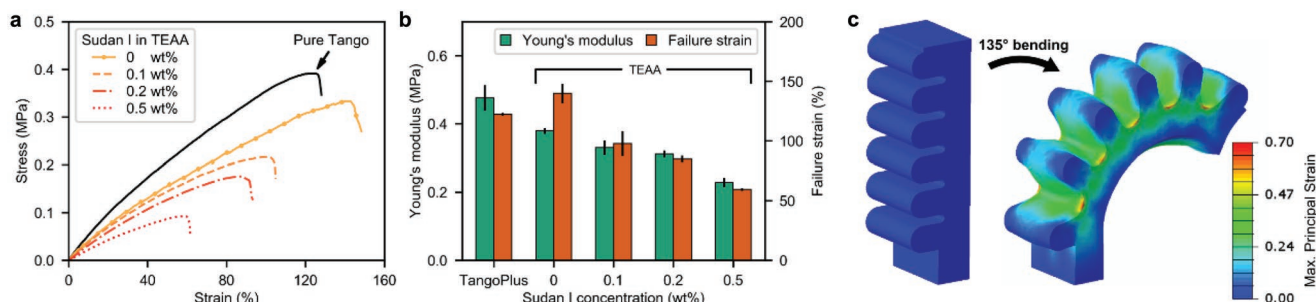
Figure 2. Characterization on mechanical properties of UV-curable elastomer with various photoabsorber concentrations. a) Stress–strain curves of tensile test results on TEAA with various Sudan I concentrations and pure TangoPlus. b) Comparison of Young's moduli and failure strains of the tested materials. c) Finite element simulation result revealing the maximum local strain induced in the actuation in Figure 1l.

In order to realize multimaterial 3D printing, we build a high-resolution, high-efficiency DLP-based 3D printing system (Figure 1e) that uses a translationally moveable polytetra-fluoroethylene (PTFE)-coated glass plate to realize fast material exchange between different puddles (Figure 1f–h).[49] An air jet cleaning process (Figure 1g) is employed to minimize polymer solution waste and contamination, and to avoid the use of cleaning solvents which may cause damage to fine features in printed parts.[54,55] By applying the tailored processing parameters to the self-built multimaterial 3D printing system, we are able to print various miniature pneumatic robots with overall size of 2–15 mm and feature size of 150–350 µm. As shown in Figure 1i, we successfully 3D printed a miniature soft pneumatic gripper with distinct voids of 190 µm in width inside the bellows (Figure 1j). The well-defined internal channels and high stretchability of the chosen UV curable elastomer ensure the functionality of the printed soft gripper which is capable of bending to the grasping gesture after a pneumatic pressure is applied (Figure 1k,l). In addition, the multimaterial printing capability of the DLP-based 3D printing system allows us to introduce material anisotropy into miniature soft robots, thus greatly enriching their actuation modes.[56] In Figure 1m, we printed a miniature soft pneumatic actuator with stiff fibers obliquely embedded in its bottom layer. The projected images and photos of the printed product are presented as insets in Figure 1f,h, respectively, for the soft matrix and stiff fibers in a multimaterial layer. Upon positive pressurization, the actuator generates a helical motion that couples bending and twisting (Figure 1n). This generic process flow offers a systematic and efficient approach to the facile tailoring of key parameters for 3D printing miniature soft pneumatic robots with high resolution and fidelity. The same methodology should be compatible with commercial stereolithography (SLA) or DLP 3D printers as long as the printing resolutions are inferior to the smallest feature sizes, as no hardware modification is required. The proposed approach paves a way to 3D printing miniature soft robots with complex geometries and sophisticated multimaterial designs.

2. Results and Discussions

2.1. Tailoring of UV-Curable Elastomer Formulation

In the current self-built DLP-based multimaterial 3D printing system, a Wintech Digital Pro6500 (Wintech Digital Systems Technology Corp., Beijing, China) is equipped as a high-resolution light engine which emits modulated UV light with 385 nm wavelength. To tailor the UV-curable elastomer formulation for 3D printing miniature soft pneumatic robots, we chose a commercially available UV curable elastomer—TangoPlus (Stratasys Ltd., Eden Prairie, MN) as the base precursor. According to our previous study, the stretchability of a UV-curable elastomer network system can be increased by adding a mono-acylate linear chain builder—epoxy aliphatic acrylate (EAA) (Ebecryl 113, Allnex, Germany).[57] In this work, we modified TangoPlus by preparing the TangoPlus-EAA (TEAA) solution with a TangoPlus-EAA weight mixing ratio of 7:3. Compared with pure TangoPlus, the addition of 30 wt% EAA leads to a reduction in Young's modulus from 0.48 to 0.38 MPa and an increase in failure strain from 120 to 140% (**Figure 2**a,b).

Based on the characterizations of the absorptivity of various commonly used photoabsorbers for DLP-based 3D printing,[46,48,52,53] we chose Sudan I (Sigma-Aldrich, St. Louis, MO) as the photoabsorber in this study due to its strong absorbance at 385 nm and sufficient solubility in a wide range of (meth)acrylate-based polymer solutions. To investigate the effect of Sudan I concentration on the mechanical performance of TEAA, we conducted uniaxial tensile tests on TEAA samples loaded with various Sudan I concentrations. Note that all the samples were 3D printed with the tailored printing parameters and further postcured in a UV oven (CL-1000 Ultraviolet crosslinker, USA) for 10 min to imitate the exposure doses received by 3D-printed miniature soft robots in their actual printing process. As shown in Figure 2a,b, the increase in Sudan I concentration from 0 to 0.5 wt% results in the decrease in both Young's modulus from 0.38 to 0.23 MPa and failure strain from 140 to 60%.

The mechanical performance characterizations facilitate the selection of appropriate photoabsorber concentration which is application dependent. For instance, a printed miniature soft pneumatic gripper (Figure 1i) requires the constituent material to be able to sustain relatively large deformation to realize the operation from the as-printed flat configuration (Figure 1k) to the inflated bent configuration (Figure 1l). The finite element simulation in Figure 2c reveals that the maximum local strain reaches 70% to complete a 135° bending under a pressure of 30 kPa for individual fingers. In practice, the gripper fingers typically burst beyond 30 kPa as measured using a manometer (Comark model C9555). From Figure 2a,b, we had to choose

TEAA with lower Sudan I concentrations (i.e., 0.1 and 0.2 wt%) based on the consideration of prioritizing the mechanical performance, even though a higher photoabsorber concentration helps to have a better control in the printing resolution.

2.2. Tailoring of Printing Parameters

For a given formulated polymer solution, good geometric fidelity in printed structures can be achieved through finding an appropriate combination of printing parameters, namely, the UV light intensity, layer thickness, and exposure time. In the current self-built DLP-based 3D printing system, the UV light intensity is set to be a constant (11.6 mW cm^{-2}). During printing, a designed structure is sliced into a series of 2D digital images that are sequentially projected at predefined vertical distances, that is, the layer thicknesses. Each digital image contains a number of isolated patterns, especially in miniature soft pneumatic robots that have microscale voids and channels (**Figure 3**a). The light engine in the 3D printer illuminates modulated UV light into the polymer resin that, due to photopolymerization, solidifies to specific patterns according to the corresponding 2D digital image. As shown in Figure 3b–d, the increase in exposure dose results in the vertical thickness growth as well as the lateral contour expansion of the printed patterns.[43,58] This photopolymerization-enabled 3D printing process can be roughly described by well-established analytical models. When a UV light is focused at the surface of a polymer solution, the curing depth C_d can be calculated by the "working curve equation"[43,58]

$$C_d = D_p \ln \left(E_{max}/E_c \right) \tag{1}$$

where E_{max} is the actual exposure dose on the surface of the polymer solution, E_c is the minimum energy needed to trigger photopolymerization, and D_p is the depth where the exposure energy decays to $1/e$ of E_{max}. Furthermore, a highly approximate model has been proposed to estimate the curing width L_w obtained by projecting a Gaussian UV light beam in a straight line of width B[58]

$$L_w = B\sqrt{C_d/2D_p} \tag{2}$$

In the case where the UV light is irradiated with a constant intensity I_{max}, E_{max} is directly proportional to the exposure time t

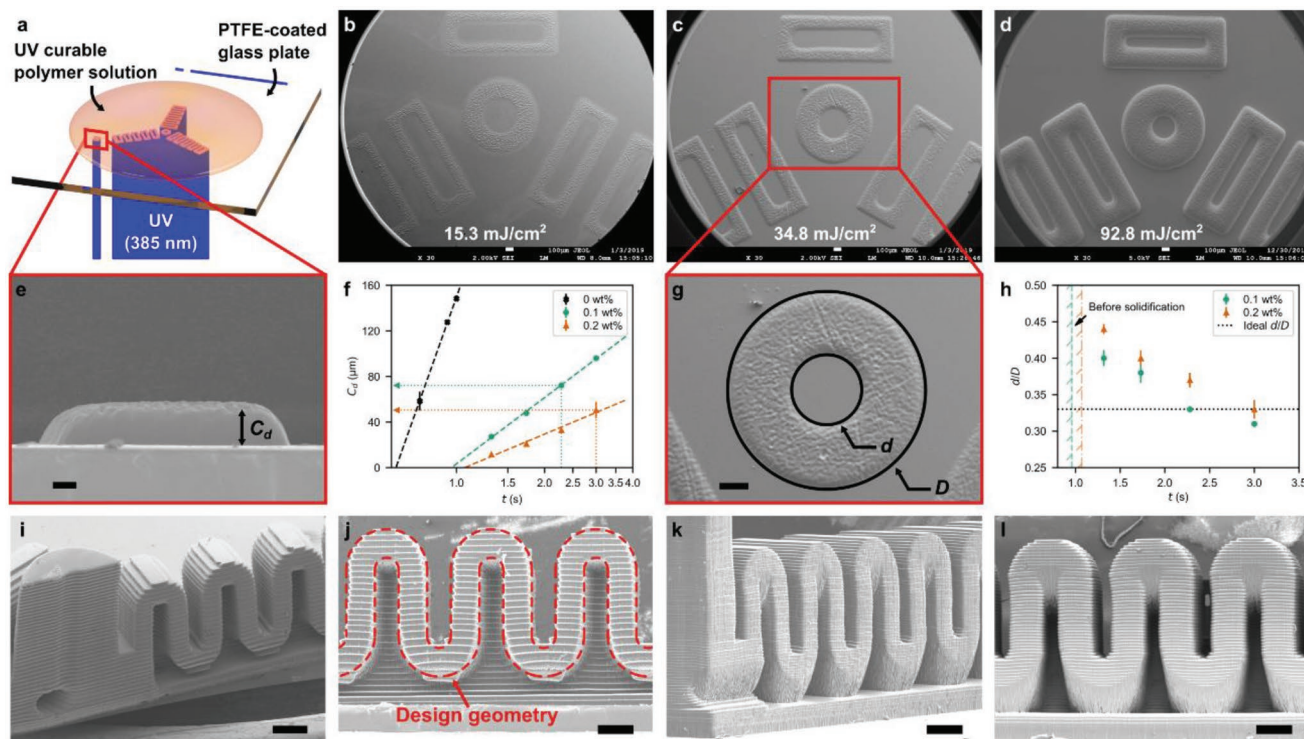$$E_{max} = I_{max}t \tag{3}$$

Figure 3. Identification of appropriate combination of exposure time and sliced layer thickness for good printing fidelity. a) Schematic illustration of the experimental setup for the characterizations of curing depth and XY fidelity. b–d) Scanning electron microscope (SEM) images of undercured, appropriately cured, and overcured patterns after a single-layer exposure. e) SEM image for the curing depth measurement. f) Measured curing depth as a function of exposure time at Sudan I concentrations of 0, 0.1, and 0.2 wt%. g) SEM image for XY fidelity characterization. The inner and outer diameters of the ring shape are, respectively, referred to as d and D. h) Measured diameter ratio d/D as a function of exposure time. The tailored exposure time should give a diameter ratio close to the ideal value. i,j) SEM images of a 3D-printed halved model of miniature soft pneumatic gripper with good geometric fidelity. The design geometry is superimposed onto the cross section of three bellows for comparison. k,l) SEM images of the same model that suffers from narrowed voids in bellows and clogged channels due to overcuring. Scale bars: (e) 40 μm; (g) 150 μm; (i)–(l) 300 μm.

ADVANCED
SCIENCE NEWS

www.advancedsciencenews.com

ADVANCED
MATERIALS
TECHNOLOGIES

www.advmattechnol.de

Integrating Equation (3) into Equation (1), the theoretical curing thickness C_d can be reexpressed as

$$C_d = D_p \ln t - D_p \ln \left(E_c / I_{max} \right) \tag{4}$$

Combining Equations (1) and (2) with Equation (3), the curing width L_w also becomes exposure time dependent

$$L_w = B \sqrt{\frac{\ln \left(I_{max} \cdot t / E_c \right)}{2}} \tag{5}$$

Therefore, the exposure time directly affects the curing depth in the vertical direction and the curing width in the lateral direction. With a proper exposure time, a good resemblance can be obtained between the cured and the designed geometries (Figure 3c). With a shorter exposure time, the patterns are undercured in the XY plane, and have thinner walls and larger voids than the designed ones (Figure 3b); with a longer exposure time, the patterns are overcured (Figure 3d). Nonetheless, controlling the printing fidelity requires not only a tailored exposure time but also an appropriate sliced layer thickness. If the sliced layer thickness is much smaller than C_d, the printed structure will experience overcuring in the vertical direction due to the excessive exposure doses received from the irradiations for curing the subsequent layers, and this overcuring will cause failure in printing microscale voids and channels. Increasing the sliced layer thickness to a value that is much greater than C_d will cause undercuring which will also lead to unsuccessful printing as the contiguous layers cannot form firm bonding with each other.

To identify the appropriate combination of exposure time and sliced layer thickness, we carried out curing depth and XY fidelity characterizations. As shown in Figure 3a, we performed these two characterizations on the same DLP-based 3D printer which was later used to print miniature soft pneumatic robots. A droplet of polymer solution was placed on the top surface of a PTFE-coated glass plate where the UV light was focused on. The printing platform was lifted so that the cured patterns had enough space to grow in the vertical direction. In the curing depth characterization, we projected a rectangular pattern (50 pixels × 50 pixels) (Figure 3a) with different exposure times and measured the resulting curing depth C_d from the vertical profiles of scanning electron microscopy (SEM) images (Figure 3e). In Figure 3f, we plotted the measured results for the TEAA samples with Sudan I concentrations of 0, 0.1, and 0.2 wt%. For the TEAA solution with a fixed Sudan I concentration, the curing depth C_d is linearly proportional to the logarithm of the exposure time t. This trend is well captured by the working curves based on Equation (4). The increase in Sudan I concentration decreases the slope of the C_d–ln t linear relation as adding more Sudan I in the TEAA solution accelerates the light intensity attenuation and leads to a shorter D_p. In addition, the increase in Sudan I concentration also shifts the intersecting point between the working curve and x-axis to a greater value as a solution with higher Sudan I concentration requires more minimal energy E_c and a longer minimal exposure time $t_c = E_c / I_{max}$ to trigger photopolymerization. We then performed XY fidelity characterization by projecting a representative sliced image (Figure 3a) of the soft pneumatic robots with different exposure times. After measuring the inner and outer diameters, respectively, denoted by d and D, of a ring shape cured by a single exposure (Figure 3g), we compared the resulting d/D ratios under different exposure times with the designed ratio (Figure 3h). This characterization method allows us to quickly identify the exposure time yielding a good XY fidelity as the opposite changes in the inner and outer diameters cause the ratio to vary obviously. A lower Sudan I concentration requires a shorter exposure time as less energy is absorbed. For TEAA with 0.1 wt% of Sudan I, the exposure time is 2.3 s; for TEAA with 0.2 wt% of Sudan I, the time is increased to 3.0 s. Using the identified exposure time, we finally located the corresponding sliced layer thickness on the working curves in Figure 3f. For TEAAs with 0.1 and 0.2 wt% of Sudan I, the appropriate sliced layer thicknesses are, respectively, 72 and 51 μm.

To demonstrate the high printing fidelity with the tailored parameters, we printed a halved model of a soft pneumatic gripper (Figure 3i) using TEAA with 0.2% Sudan I. The tailored exposure time and sliced layer thickness were 3.0 s and 50 μm, respectively. Figure 3j presents an SEM image which clearly shows that the voids and channels were successfully printed without clogging. We further compared the cross-sectional area of the three printed bellows in Figure 3j with the designed area. The printed area is about 94% of the designed one indicating that using the appropriate combination of printing parameters ensures a high printing fidelity. The generic process flow proposed in the manuscript offers a systematic and efficient approach to quickly identify the tailored key parameters for 3D printing miniature soft pneumatic robots with high resolution and fidelity. Without those tailored key parameters, the printed products may suffer from narrowed voids in bellows and clogged channels (Figure 3k,l) due to overcuring.

2.3. Demonstrations of 3D-Printed Miniature Soft Pneumatic Robots

We were able to 3D print miniature soft pneumatic robots with various designs by tailoring the printing parameters via the aforementioned methods. An assortment of soft robot designs were selected from the literature, and a miniaturized version of each design was successfully printed in one single step. **Figure 4**a shows a miniature multigait soft robot with three independent pneumatic networks controlling the two forelimbs, the main body, and the two hindlimbs, respectively.[59] Actuating the pneumatic networks simultaneously with positive pressurization causes the robot body to be lifted from the surface which is an intermediate step in crawling. Figure 4b displays a miniature soft actuator where the bellows are obliquely arranged, and that is capable of bending and twisting in a helical manner under positive or negative pressurization.[60,61] Figure 4c demonstrates a miniature soft linear actuator that functions based on buckling induced by negative pressurization.[62] These examples illustrate the printed results of soft robots with voids and channels arranged planarly in the lateral direction and with a single material. Apart from that, DLP-based 3D printing also offers the capability to print miniature soft robots with higher geometric complexity and multiple materials. Figure 4d presents a miniature soft gripper which remains closed in the rest
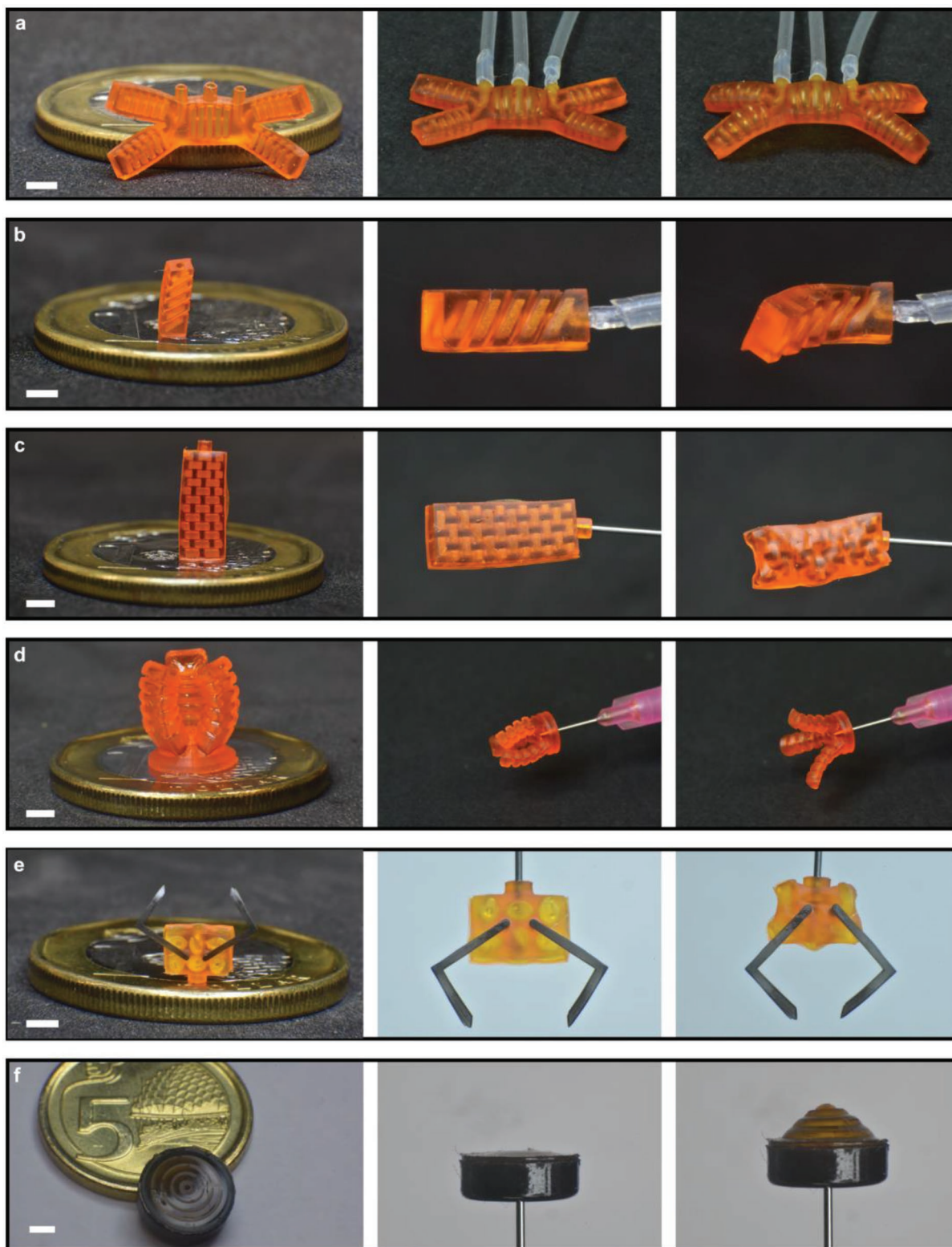
**ADVANCED
SCIENCE NEWS**

www.advancedsciencenews.com

**ADVANCED
MATERIALS
TECHNOLOGIES**

www.advmattechnol.de

Figure 4. An assortment of printed miniature soft robot prototypes which are inspired by the literature. Each subfigure shows, from left to right, still images of the printed soft robot placed on a 1 Singapore Dollar coin (a 5 cent coin for the last one), the robot before and after pneumatic actuation. a) A miniature multigait soft robot that lifts its body upon positive pressurization.[59] b) A miniature soft helical actuator that actions under positive or negative pressurization.[60,61] c) A miniature soft actuator that provides linear motion under negative pressurization.[62] d) A miniature soft gripper with a nonplanar design.[36] e) A miniature multimaterial soft gripper comprising a soft actuator and two stiff claws.[63] f) A miniature soft inflatable surface that could enable camouflage in soft robotic systems.[64] Scale bars: (a)–(f) 2 mm.
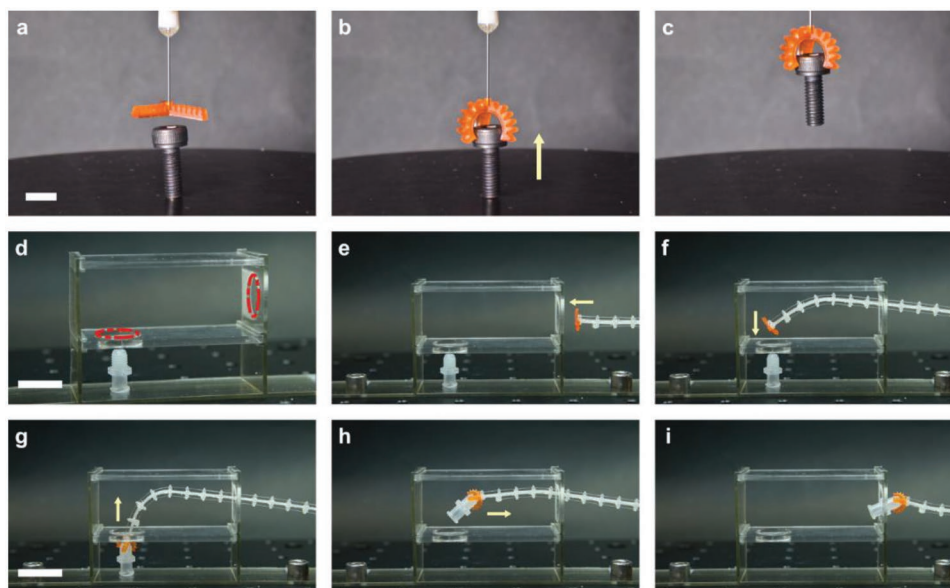
**ADVANCED
SCIENCE NEWS**
www.advancedsciencenews.com

**ADVANCED
MATERIALS
TECHNOLOGIES**
www.advmattechnol.de

Figure 5. Demonstration of debris removal in a confined space by combining a miniature soft pneumatic gripper and a continuum manipulator. a–c) A preliminary test showing the gripper's capability of conforming to a target object and providing sufficient block force to firmly grasp and lift the object. d) The experiment setup to simulate the real-life situation of debris removal in a hard-to-reach position. e–i) Real images of the soft debris remover navigating through two holes (one horizontal and the other vertical) to approach the target object, grasping and lifting the object, and exiting the structure while holding the object. Scale bars: (a) 5 mm; (d) 2 cm; (g) 2 cm.

state and opens upon positive pressurization.[36] Due to the rather vertical arrangement of the fingers, the use of tailored printing parameters is critical to ensure that the voids are still printed with good fidelity even though the slicing direction is different from that of planar designs as studied in Figure 3. Figure 4e shows a miniature gripper made of both soft and stiff materials.[63] The soft material, that is, TEAA in this example, was used to print a buckling actuator. Two stiff claws (black in Figure 4e) were printed on the surface of the actuator's center area. Negative pressurization induces rotary motions on the claws and causes them to close up. Finally, Figure 4f illustrates a miniature soft inflatable surface with embedded inextensible stiff meshes that restrict the surface to normal displacement upon positive pressurization.[64] This approach could be used to enable camouflage in miniature soft robotic systems. In this example, the stiff meshes (black in Figure 4f) are a series of concentric rings and are printed in the same plane as the soft material.

2.4. Application Demonstration of a 3D-Printed Miniature Soft Robot

To demonstrate the potential application of 3D-printed miniature soft pneumatic robots, we devised a soft debris remover that could navigate in a confined space and collect small objects in a hard-to-reach position. The soft robot comprises a continuum manipulator and a 3D-printed miniature soft pneumatic gripper, respectively, used for the navigation and grasping tasks. A preliminary test was conducted to show the gripper's capability of conforming to a target object and providing sufficient block force to firmly grasp and lift the object

(**Figure 5**a–c and Movie S1, Supporting Information). Next, we built a mockup to simulate the real-life situation of debris removal from within a plane engine. When small objects are ingested into engines, serious damage may be caused. However, tools made of rigid materials are not always suitable due to lack of flexibility and safety. For example, to remove the target object which is trapped in a structure as shown in Figure 5d, we need a tool that can navigate through two holes (highlighted in red in Figure 5d) and grasp the object without causing collateral damage to the structure. To this end, we fabricated a continuum manipulator, passed a soft tubing through its spine, and connected a 3D-printed miniature gripper to the tubing near the tip of the manipulator. By controlling the latter, we were able to send the gripper close to the object (Figure 5e,f and Movie S2, Supporting Information). We then operated the gripper to conform to the object (Figure 5g) and held the pressure to carry the object while navigating with the manipulator to exit the structure (Figure 5h,i).

3. Conclusion

In summary, we present a generic process flow that instructs the manufacturing of miniature pneumatic actuators for soft robots using the DLP-based multimaterial 3D printing technology. Without prior knowledge of the appropriate combination of material formulation and processing parameters, fabricating soft pneumatic robots at millimeter scale with microscale voids and channels and capable of undergoing large deformations has been challenging. To tailor the material formulation, we select the appropriate type of photoabsorber based on its absorbance at wavelength of the projected UV light and

**ADVANCED
SCIENCE NEWS**

www.advancedsciencenews.com

**ADVANCED
MATERIALS
TECHNOLOGIES**

www.advmattechnol.de

investigate the effect of its concentration on the mechanical performance of the material. The appropriate combination of exposure time and sliced layer thickness is identified according to characterizations for curing depth and XY fidelity. We have demonstrated that applying the tailored material formulation and key processing parameters results in successful printing of an assortment of geometrically complex designs of miniature soft pneumatic robots (Figure 4a–e). In addition, by introducing material anisotropy with the multimaterial printing capability, we could fabricate mechanically complex structures to enrich the morphing modes of miniature soft robots (Figure 1m,n) or impart them with more functionalities such as camouflage (Figure 4f). The integration of printed miniature soft pneumatic actuators into a robotic system offers potential applications such as jet-engine maintenance (Figure 5) and minimally invasive surgery.

4. Experimental Section

Polymer Solution Preparation: The base precursor of the UV-curable elastomer, TangoPlus, was purchased from Stratasys (MN, USA). EAA (Ebecryl 113) was chosen as the mono-acylate linear chain builder and was purchased from Allnex (Germany). Sudan I which was used as the photoabsorber for DLP-based 3D printing was purchased from Sigma-Aldrich (MO, USA). All the materials were used as received. The UV-curable elastomer TEAA for 3D printing was prepared by mixing TangoPlus and TEAA in a 7:3 weight ratio. The mixtures were stirred on a magnetic stirrer for about 2 h and then degassed. Sudan I (0.1–0.5 wt% of the total solution) was added to the TEAA solution at room temperature.

Mechanical Performance Characterization: Uniaxial tensile tests were performed to characterize the Young's moduli and the failure strains of printed TEAA samples loaded with different Sudan I concentrations as well as printed pure TangoPlus samples at room temperature. These mechanical properties were measured on an MTS uniaxial tensile testing machine (Criterion Model 43, MN, USA) with a 100 N load cell under 0.1 mm s^{-1} strain rate. The dimensions of the specimens are 15 mm × 4 mm × 1 mm.

Finite Element Simulation: To determine the maximum local strain on the actuated miniature soft robotic gripper, a finite element simulation was performed on one finger of the gripper using a commercial software ABAQUS (Dassault Systèmes Simulia Corp., Providence, RI). The geometries were meshed using four-node linear tetrahedron and hybrid elements (C3D4H) for the whole printed structure. The Mooney–Rivlin model was used to capture the hyperelastic behavior of TEAA with 0.2 wt% Sudan I. Assuming incompressibility of the material, the form of the Mooney–Rivlin strain energy potential is given by $U = C_{10}(\overline{I_1} - 3) + C_{01}(\overline{I_2} - 3)$ where U is the strain energy density, C_{10} and C_{01} are material parameters, and $\overline{I_1}$ and $\overline{I_2}$ are the principal invariants. By fitting the stress–strain curve, $C_{10} = 0.0566$ MPa and $C_{01} = 0.0033$ MPa were obtained. Boundary conditions were applied to fix the finger at the air inlet. A uniform pressure was applied onto the inner surface of the voids.

DLP-Based Multimaterial 3D Printing System: A self-built DLP-based multimaterial 3D printing system[49] was used to fabricate the miniature soft pneumatic robots. Puddles of UV-curable polymer solutions were placed on a borosilicate glass plate (Borofloat 33, Schott AG, Mainz, Germany, 93% UV transmission) covered with optically clear PTFE silicone-adhesive tape (CS Hyde, Lake Villa, IL). The plate was horizontally translated using a translational stage (LTS150, Thorlabs, Inc., Newton, NJ) to enable rapid material exchange. Customized 385 nm wavelength UV patterns were projected upward using a DLP light engine (Pro6500, Wintech Digital Systems Technology Corp., Beijing, China), resulting in a lateral resolution of 9.3 μm. The prints

were formed on a printing platform which is vertically controlled by a translational stage (LTS300, Thorlabs, Inc., Newton, NJ) with 0.1 μm achievable increment. The material exchange step includes an air jet cleaning process using a high-precision dispenser (Ultimus V, Nordson EFD, Nordson, OH).

Light Intensity Characterization: The light intensity emitted by the light source at the focal plane was measured using a radiometer (ILT2400, International Light Technologies, Peabody, MA). The spectral range of the device lies between 275 and 450 nm. The sensing area is smaller than the projection area of the DLP-based 3D printing system. During the measurement, the sensing area was placed in the middle of the projection area.

Scanning Electron Microscopy: SEM was used to analyze the microstructure of the samples. SEM images were acquired on a Hitachi SU8010 SEM (Hitachi Ltd., Chiyoda, Tokyo, Japan). The samples were attached to a SEM holder and then gold-sputtered in vacuum before test.

Printing Fidelity Estimation: The overall geometric fidelity in both lateral and vertical directions was estimated by calculating the cross-sectional area ratio between a group of three printed bellows and the corresponding design geometry. A Python script was written to convert the SEM image shown in Figure 3j into grayscale and image thresholding was performed to set all the pixels outside the cross sections to black (0). The numbers of nonzero pixels were then counted to calculate the printed cross-sectional area.

Supporting Information

Supporting Information is available from the Wiley Online Library or from the author.

Conflict of Interest

The authors declare no conflict of interest.

Keywords

[1] D. Rus, M. T. Tolley, *Nature* **2015**, *521*, 467.
[2] M. Wehner, R. L. Truby, D. J. Fitzgerald, B. Mosadegh, G. M. Whitesides, J. A. Lewis, R. J. Wood, *Nature* **2016**, *536*, 451.
[3] M. T. Tolley, R. F. Shepherd, B. Mosadegh, K. C. Galloway, M. Wehner, M. Karpelson, R. J. Wood, G. M. Whitesides, *Soft Rob.* **2014**, *1*, 213.

[4] E. W. Hawkes, L. H. Blumenschein, J. D. Greer, A. M. Okamura, *Sci. Rob.* **2017**, *2*, eaan3028.

[5] Y. F. Zhang, N. Zhang, H. Hingorani, N. Ding, D. Wang, C. Yuan, B. Zhang, G. Gu, Q. Ge, *Adv. Funct. Mater.* **2019**, *29*, 1806698.

[6] B. Mosadegh, P. Polygerinos, C. Keplinger, S. Wennstedt, R. F. Shepherd, U. Gupta, J. Shim, K. Bertoldi, C. J. Walsh, G. M. Whitesides, *Adv. Funct. Mater.* **2014**, *24*, 2163.

[7] N. W. Bartlett, M. T. Tolley, J. T. B. Overvelde, J. C. Weaver, B. Mosadegh, K. Bertoldi, G. M. Whitesides, R. J. Wood, *Science* **2015**, *349*, 161.

[8] A. S. Gladman, E. A. Matsumoto, R. G. Nuzzo, L. Mahadevan, J. A. Lewis, *Nat. Mater.* **2016**, *15*, 413.

[9] H. Yuk, S. T. Lin, C. Ma, M. Takaffoli, N. X. Fang, X. H. Zhao, *Nat. Commun.* **2017**, *8*, 14230.

[10] Y. Kim, H. Yuk, R. K. Zhao, S. A. Chester, X. H. Zhao, *Nature* **2018**, *558*, 274.

[11] H. Y. Jia, E. Mailand, J. T. Zhou, Z. J. Huang, G. Dietler, J. M. Kolinski, X. L. Wang, M. S. Sakar, *Small* **2019**, *15*, 1803870.

[12] G. Y. Gu, J. Zou, R. K. Zhao, X. H. Zhao, X. Y. Zhu, *Sci. Rob.* **2018**, *3*, eaat2874.

[13] C. M. Boutry, M. Negre, M. Jorda, O. Vardoulis, A. Chortos, O. Khatib, Z. N. Bao, *Sci. Rob.* **2018**, *3*, eaau6914.

[14] G. Gu, H. Xu, S. Peng, L. Li, S. Chen, T. Lu, X. Guo, *Soft Rob.* **2019**, *6*, 368.

[15] H. W. Huang, T. Y. Huang, M. Charilaou, S. Lyttle, Q. Zhang, S. Pane, B. J. Nelson, *Adv. Funct. Mater.* **2018**, *28*, 1802110.

[16] M. Power, A. J. Thompson, S. Anastasova, G. Z. Yang, *Small* **2018**, *14*, 1703964.

[17] W. Hu, G. Z. Lum, M. Mastrangeli, M. Sitti, *Nature* **2018**, *554*, 81.

[18] M. De Volder, D. Reynaerts, *J. Micromech. Microeng.* **2010**, *20*, 043001.

[19] L. Hines, K. Petersen, G. Z. Lum, M. Sitti, *Adv. Mater.* **2017**, *29*, 1603483.

[20] M. Sitti, *Nat. Rev. Mater.* **2018**, *3*, 74.

[21] B. Gorissen, D. Reynaerts, S. Konishi, K. Yoshida, J. W. Kim, M. De Volder, *Adv. Mater.* **2017**, *29*, 1604977.

[22] S. Konishi, M. Nokata, O. C. Jeong, S. Kusuda, T. Sakakibara, W. Kuwayama, H. Tsutsumi, presented at 2006 IEEE Int. Conf. Robotics and Automation (ICRA), Orlando, FL, May **2006**.

[23] B. Gorissen, M. De Volder, A. De Greef, D. Reynaerts, *Sens. Actuators, A* **2011**, *168*, 58.

[24] B. C. M. Chang, J. Berring, M. Venkataram, C. Menon, M. Parameswaran, *Smart Mater. Struct.* **2011**, *20*, 035012.

[25] S. Wakimoto, K. Suzumori, K. Ogura, *Adv. Rob.* **2011**, *25*, 1311.

[26] B. Gorissen, W. Vincentie, F. Al-Bender, D. Reynaerts, M. De Volder, *J. Micromech. Microeng.* **2013**, *23*, 045012.

[27] B. Gorissen, T. Chishiro, S. Shimomura, D. Reynaerts, M. De Volder, S. Konishi, *Sens. Actuators, A* **2014**, *216*, 426.

[28] Y. Hwang, O. H. Paydar, R. N. Candler, *Sens. Actuators, A* **2015**, *234*, 65.

[29] J. W. Paek, I. Cho, J. Y. Kim, *Sci. Rep.* **2015**, *5*, 10768.

[30] Y. Sun, S. Song, X. Q. Liang, H. L. Ren, *IEEE Rob. Autom. Lett.* **2016**, *1*, 617.

[31] M. De Volder, A. J. M. Moers, D. Reynaerts, *Sens. Actuators, A* **2011**, *166*, 111.

[32] S. Russo, T. Ranzani, C. J. Walsh, R. J. Wood, *Adv. Mater. Technol.* **2017**, *2*, 1700135.

[33] N. R. Sinatra, T. Ranzani, J. J. Vlassak, K. K. Parker, R. J. Wood, *J. Micromech. Microeng.* **2018**, *28*, 084002.

[34] T. Ranzani, S. Russo, N. W. Bartlett, M. Wehner, R. J. Wood, *Adv. Mater.* **2018**, *30*, 1802739.

[35] B. N. Peele, T. J. Wallin, H. C. Zhao, R. F. Shepherd, *Bioinspiration Biomimetics* **2015**, *10*, 055003.

[36] D. K. Patel, A. H. Sakhaei, M. Layani, B. Zhang, Q. Ge, S. Magdassi, *Adv. Mater.* **2017**, *29*, 1606000.

[37] D. Drotman, S. Jadhav, M. Karimi, P. deZonia, M. T. Tolley, presented at 2017 IEEE Int. Conf. Robotics and Automation (ICRA), Singapore, Singapore, May **2017**.

[38] R. L. Truby, M. Wehner, A. K. Grosskopf, D. M. Vogt, S. G. M. Uzel, R. J. Wood, J. A. Lewis, *Adv. Mater.* **2018**, *30*, 1706383.

[39] M. Schaffner, J. A. Faber, L. Pianegonda, P. A. Ruhs, F. Coulter, A. R. Studart, *Nat. Commun.* **2018**, *9*, 878.

[40] L. S. Ge, L. T. Dong, D. Wang, Q. Ge, G. Y. Gu, *Sens. Actuators, A* **2018**, *273*, 285.

[41] K. Suzumori, A. Koga, H. Riyoko, presented at 1994 IEEE Micro Electro Mechanical Systems, Oiso, Japan, January **1994**.

[42] H. W. Kang, I. H. Lee, D. W. Cho, *Microelectron. Eng.* **2006**, *83*, 1201.

[43] C. Sun, N. Fang, D. M. Wu, X. Zhang, *Sens. Actuators, A* **2005**, *121*, 113.

[44] J. R. Tumbleston, D. Shirvanyants, N. Ermoshkin, R. Janusziewicz, A. R. Johnson, D. Kelly, K. Chen, R. Pinschmidt, J. P. Rolland, A. Ermoshkin, E. T. Samulski, J. M. DeSimone, *Science* **2015**, *347*, 1349.

[45] Q. Ge, A. H. Sakhaei, H. Lee, C. K. Dunn, N. X. Fang, M. L. Dunn, *Sci. Rep.* **2016**, *6*, 31110.

[46] H. Gong, M. Beauchamp, S. Perry, A. T. Woolley, G. P. Nordin, *RSC Adv.* **2015**, *5*, 106621.

[47] C. I. Rogers, K. Qaderi, A. T. Woolley, G. P. Nordin, *Biomicrofluidics* **2015**, *9*, 016501.

[48] H. Gong, B. P. Bickham, A. T. Woolley, G. P. Nordin, *Lab Chip* **2017**, *17*, 2899.

[49] K. Kowsari, S. Akbari, D. Wang, N. X. Fang, Q. Ge, *3D Print. Addit. Manuf.* **2018**, *5*, 185.

[50] C. Zhou, Y. Chen, Z. Yang, B. Khoshnevis, presented at 2011 Annual Solid Freeform Fabrication Symp., Austin, TX, August **2011**.

[51] C. Zhou, Y. Chen, *J. Manuf. Processes* **2012**, *14*, 107.

[52] K. Kowsari, B. Zhang, S. Panjwani, Z. C. Chen, H. Hingorani, S. Akbari, N. X. Fang, Q. Ge, *Addit. Manuf.* **2018**, *24*, 627.

[53] N. Bhattacharjee, C. Parra-Cabrera, Y. T. Kim, A. P. Kuo, A. Folch, *Adv. Mater.* **2018**, *30*, 1800001.

[54] J. W. Choi, H. C. Kim, R. Wicker, *J. Mater. Process. Technol.* **2011**, *211*, 318.

[55] C. Zhou, Y. Chen, Z. G. Yang, B. Khoshnevis, *Rapid Prototyping J.* **2013**, *19*, 153.

[56] D. Wang, L. Li, A. Serjouei, L. T. Dong, O. Weeger, G. Y. Gu, Q. Ge, *Appl. Phys. Lett.* **2018**, *112*, 181905.

[57] H. Hingorani, Y.-F. Zhang, B. Zhang, A. Serjouei, Q. Ge, *Int. J. Smart Nano Mater.* **2019**, *10*, 225.

[58] P. F. Jacobs, *Rapid Prototyping and Manufacturing: Fundamentals of StereoLithography*, McGraw-Hill, New York **1993**.

[59] R. F. Shepherd, F. Ilievski, W. Choi, S. A. Morin, A. A. Stokes, A. D. Mazzeo, X. Chen, M. Wang, G. M. Whitesides, *Proc. Natl. Acad. Sci. USA* **2011**, *108*, 20400.

[60] T. Y. Wang, L. S. Ge, G. Y. Gu, *Sens. Actuators, A* **2018**, *271*, 131.

[61] W. P. Hu, W. H. Li, G. Alici, presented at 2018 IEEE/ASME Int. Conf. Advanced Intelligent Mechatronics (AIM), Auckland, New Zealand, July **2008**.

[62] D. Yang, M. S. Verma, J. H. So, B. Mosadegh, C. Keplinger, B. Lee, F. Khashai, E. Lossner, Z. G. Suo, G. M. Whitesides, *Adv. Mater. Technol.* **2016**, *1*, 1600055.

[63] D. Yang, B. Mosadegh, A. Ainla, B. Lee, F. Khashai, Z. G. Suo, K. Bertoldi, G. M. Whitesides, *Adv. Mater.* **2015**, *27*, 6323.

[64] J. H. Pikul, S. Li, H. Bai, R. T. Hanlon, I. Cohen, R. F. Shepherd, *Science* **2017**, *358*, 210.